Journal of Materials Chemistry A

ARTICLE

Coordination effect of network NiO nanosheet and a carbon layer on the cathode side in constructing a high-performance lithium-sulfur battery

Received 00th January 20xx,
Accepted 00th January 20xx

DOI: 10.1039/x0xx00000x

www.rsc.org/

Jie Wang,[a,b] Jianing Liang,[a] Jianzhong Wu,[a] Cuijuan Xuan,[a] Xuyun Guo,[b] Chenglong Lai,[a] Ye Zhu,[b] Deli Wang[a,*]

Effectively entrapping polysulfides from dissolution during discharging/charging process to improve the performance for a lithium-sulfur battery is one of an essential unit for commercialization process. NiO sheet with network structure is developed via simple two-step method and used as mediation for lithium-sulfur battery coupled with a carbon layer on the cathode side. Specifically, by introducing a thin carbon layer on the cathode side of the separator, the dissolution of polysulfides is effectively hindered, meanwhile, the rate capability and long-term stability is effectively enhanced by further addition of network NiO nanosheets due to the mesoporous channel and the NiO-S interaction. Besides, compared with the cell performance of different S loading, the cathode with 80 wt% of S in the total electrode exhibited a high specific capacity and excellent rate performance up to 5 C. In addition, although the redox potential range of NiO is not involved in the rechargeable potential window, NiO exhibit obvious interaction with polysulfides and restricted its dissolution tendency. The present study demonstrates that the joint action of network NiO and carbon layer present great potential to be used in low-cost and high-energy lithium sulfur batteries and provides important guidance to the design of a multi-functional sulfur host for the battery cathodes.

Introduction

Rechargeable lithium-sulfur (Li-S) batteries, delivering a high theoretical capacity of 1675 mA h g^{-1} and energy density of 2500 kW kg^{-1} (~ six fold of commercial $LiCoO_2$/C cell), have attracted increasingly attention,[1-3] which are recognized as one of the most promising candidates to satisfy emerging market. Sulfur, serve as the indispensable cathode material, possesses low competitive cost, natural abundance in resource and environmental friendly merits.[3-5] In Addition, when coupled with Li metal anode, the battery operates at a safer voltage of ~2.15 V (vs Li^+/Li) compared with conventional Li-insertion compounds (~3-4.5 V versus Li^+/Li), and offers a higher energy density than thionic counterparts.[6] According to the facts of advantages, Li-S battery should be capable of energy storage times longer than lithium ion batteries as well as other energy conversion and storage devices.[7] However, Li-S batteries are also facing several obstacles which significantly influence the electrochemical performance of all aspects. (i) The insulating nature of sulfur and lithium sulfides, lead to low utilization of sulfur, poor electrochemical activity and even lowers the Coulombic efficiency, which require addition of conductive or interactive mediates.[8] (ii) The formation of lithium polysulfides during the discharge/charge process would dissolve in organic electrolytes and are suspected to "shuttle" between the electrodes, resulting in a rapid fading of capacity and high self-discharge.[9] Therefore, developing active materials to entrap polysulfides from dissolution and enhance the utility of sulfur are facing great challenge.

Over decades, numerous efforts have been devoted to address these issues by trapping the polysulfides within the cathode side. Among these strategies, encapsulate sulfur in the pores of carbon materials or conductive polymer matrix has been used as an efficient common approach. Carbon materials with meso/microporous structure,[10-14] hollow carbon spheres,[15-17] carbon nanotubes/fibres[18-22] and conductive polymers sulfur-host cathodes[23-25] have exhibited positive effects on stabilize the cycling performance of Li-S cell. However, the above mentioned carbon based materials can only partially retain polysulfides physically and would gradually lose the effects over time due to the structural changes that arise from the over 80% volume change of the sulfur cathode on discharge.[26, 27] Thus, it is of vital importance to design an electrode could not only enhance the electrochemical

[a] Key Laboratory of Material Chemistry for Energy Conversion and Storage (Huazhong University of Science and Technology), Ministry of Education, Hubei Key Laboratory of Material Chemistry and Service Failure, School of Chemistry and Chemical Engineering, Huazhong University of Science and Technology, Wuhan, 430074, P.R. China. E-mail: wangdl81125@hust.edu.cn.
[b] Department of Applied Physics, The Hong Kong Polytechnic University, Hung Horn, Kowloon, Hong Kong.

Electronic Supplementary Information (ESI) available: [details of XRD patterns, TEM images, TGA curves and additional electrochemical performance]. See DOI: 10.1039/x0xx00000x

The following publication Wang, J., Liang, J., Wu, J., Xuan, C., Wu, Z., Guo, X., . . . Wang, D. (2018). Coordination effect of network NiO nanosheet and a carbon layer on the cathode side in constructing a high-performance lithium-sulfur battery. Journal of Materials Chemistry A, 6(15), 6503-6509 is available at https://doi.org/10.1039/c8ta00270c.

processes of S but also effectively entrap the intermediate polysulfide during high-rate discharge/charge process. Recently, chemical mediator[28-30] and carbon coating method[31-34] have been proposed to prevent the polysulfides from dissolution which effectively maintained the high-capacity retention. In the above mentioned mediator, such as MnO_2, have shown characteristic redox peaks between the discharge/charge potential window which would interact with polysulfides to form insoluble large thiosulfate clusters and be isolated at cathodic side.[30, 35] In addition, the polysulfides would be held back on the cathode via a carbon coating on the separator membrane which effectively restricted the "shuttle" of dissolved polysulfides. Therefore, combination of the two new strategies to further stable the Li–S battery system would not only expect to enhance the utility od sulfur, but also extend the battery cycling life.

Herein, network NiO nanosheets was successfully prepared and served as a mediator, which coupled with a carbon layer at the cathode side of the separator and operate in high-rate rechargeable Li-S battery. During the operation of a battery, the carbon layer prevented the polysulfides from shuttling, which effectively enhanced the cycling stability. Meanwhile, the mesoporous pores and the ultra-thin sheet layer not only provided enough channels for the intimate contact between electrolyte and sulfur, but also adequate surface area to accommodate sulfur, which largely improved the utility of sulfur and reflected in the excellent capacity at high discharging/charging rates. The network NiO nanosheets sample with 80% mass S accommodation exhibited the highest capacity and excellent capacity retention at 0.2 C, compared with the network NiO nanosheets sample with S loading of 60%, 40%, 20% and pure S. In addition, it maintained a stable cycling performance at 2 C and 5 C over 300 cycles with nearly 100% Coulombic efficiency.

Experimental Section

Synthesis of network NiO Nanosheets (NNN).

The synthetic procedure of network NiO nanosheets was via a simple two-step method.[36] Firstly, sheet-like Ni-based precursor was prepared by hydrothermal process. 1 mmol nickel acetate and 2 mmol hexamethylenetetramine (HMT) were dissolved in 40 mL of distilled water under magnetic stirring for 1 h to form a homogenous solution. Then the mixture was transferred into a 50 mL Teflon-lined autoclave, sealed and heated at 110 ℃ for 12 h. After cooled down to room temperature, the hydrothermal product was collected by centrifuging with a mixture of ultra-pure water and ethanol for several times, and then dried under freeze drying to ensure adequate drying. Secondly, the NNN sample were obtained via simple calcination in air from room temperature to 500 ℃ at a heating rate of 10 ℃ min^{-1} and maintained for 3 h.

Preparation of network NiO nanosheets sample with different S loading

Typical for network NiO nanosheets sample with 80 wt% S loading, the composite was prepared following a melt-diffusion strategy as follows: 100 mg S_8 powders and 25 mg NNN sample was grinded in agate mortal and then transferred into a 50 mL sealed Teflon-lined autoclave and held at a 155 ℃ oven for 12 h. The as-obtained composite was denoted as NNN-S80, while the NNN-S60, NNN-S40 and NNN-S20 were prepared by using the same method.

Physical characterization

Field emission scanning electron microscopy images were obtained via Nova NanoSEM 450. Transmission electron microscopy (TEM), high-resolution TEM (HRTEM), scanning transmission electron microscopy (STEM) and high-angle annular dark field STEM (HAADF-STEM) images were recorded via JEOL JEM-2100F. Energy dispersive spectra mapping images were obtained by using JEOL JEM-2100F equipped with INCA Energy spectrometer. Powder X-ray diffraction (XRD) analysis was performed by using an X'Pert PRO diffractometer using Cu Kα (λ = 1.5406 Å) radiation, and diffraction patterns were collected at scanning rate of 4 ℃ min^{-1}. Thermal gravimetric analysis (TGA) was conducted on TA-Q500 TGA instrument at a heating rate of 10 °C min^{-1}. X-ray photoelectron spectroscopy (XPS) was conducted by using an AXIS-ULTRA DLD-600W Instrument.

Electrochemical measurements

The NNN-S80 composite was combined with conductive carbon (super-p) and polymer binder (polyvinylidene fluoride; PVDF) in a mass ratio of 80:10:10 and milled into a slurry with N-methylpyrrolidone. The slurry was then blade cast onto an Al foil and dried at 55 ℃ for 12 h in a vacuum oven. The specific loading density of sulfur was ca. 2.18 mg cm^{-2}. CR2032 coin cells were assembled in an argon-filled glove box employing the NNN-S80-coated Al foil as the cathode, a carbon-coated porous membrane (Celgard 3320) as the separator, and lithium foil as the reference/counter electrode. The electrolyte was used by comprising 1M LiTFSI in a 1:1 volume of DME : DOL with 2 wt% $LiNO_3$. Specific capacity values were calculated with respect to the mass of sulfur. Cyclic voltammetry curves (CV) were collected using a CHI 1040C electrochemical workstation at a scan rate of 0.05 mV s^{-1} from 3.0 to 1.5 V. Cycling tests of the batteries were galvanostatically performed at various discharge/charge rates within a potential window between 1.5 and 3.0 V versus Li^+/Li. Electrochemical impedance spectroscopy (EIS) measured on the coin cell was performed with an Autolab PG302N electrochemical workstation in the frequency range from 100 kHz to 0.01 Hz at open circuit potential.

Results and discussion

The synthetic procedure of NNN sample was described into a simple two-step method. Firstly, sheet-like Ni-based precursor was prepared by hydrothermal process. As can be seen from the SEM image in Fig. 1(a), the Ni-based precursor exhibits micro-size scale sheet, ultrathin vertical thickness (~ 10 nm) and smooth surface structure. After calcined in air at 500 ℃, the Ni-based precursor was

oxidized and transformed into NiO which can be verified by XRD characterization (Fig. S1) and the electron energy loss spectrum (Fig. S2b). The diffraction peaks at 37.4°, 43.4°, 63.2°, 75.4° and 79.9° are corresponding to the (111), (200), (220), (311) and (222) plane, consistent with the standard cubic NiO (Reference code: 00-001-1239). Moreover, as can be seen from the SEM image (Fig. 1b and Fig. S2a), the NiO still maintained the sheet-shape structure, but the smooth surface converted to rough. Furtherly, the HAADF-STEM image (inset of Fig. 1c) shows an enlarged magnification of a selected area which showed ultra-thin sheets with porous pores on it. By measuring the pore size (white dashed outline) from the enlarged TEM (Fig. 1c) image, the NNN were verified to possess mesoporous structure. The mesopores would facilitate the electrolyte penetration and immersion,[37] while the network structure could enhance the polysulfide electrolyte impregnation and then effectively stores the active material in the through its strong absorption.[11, 38] The HRTEM image and corresponding fast Fourier transform (FFT) pattern in Fig. 1d clearly reveal that the nanosheet is a hexagonal single crystal with c-axis crystalline orientation, where the inter-planar spacing between adjacent fringes are measured to be 0.15 nm from two orientations, corresponding to the (220) plane. The excellent crystal structure would ensure its stability during discharge/charge process for a Li-S battery.

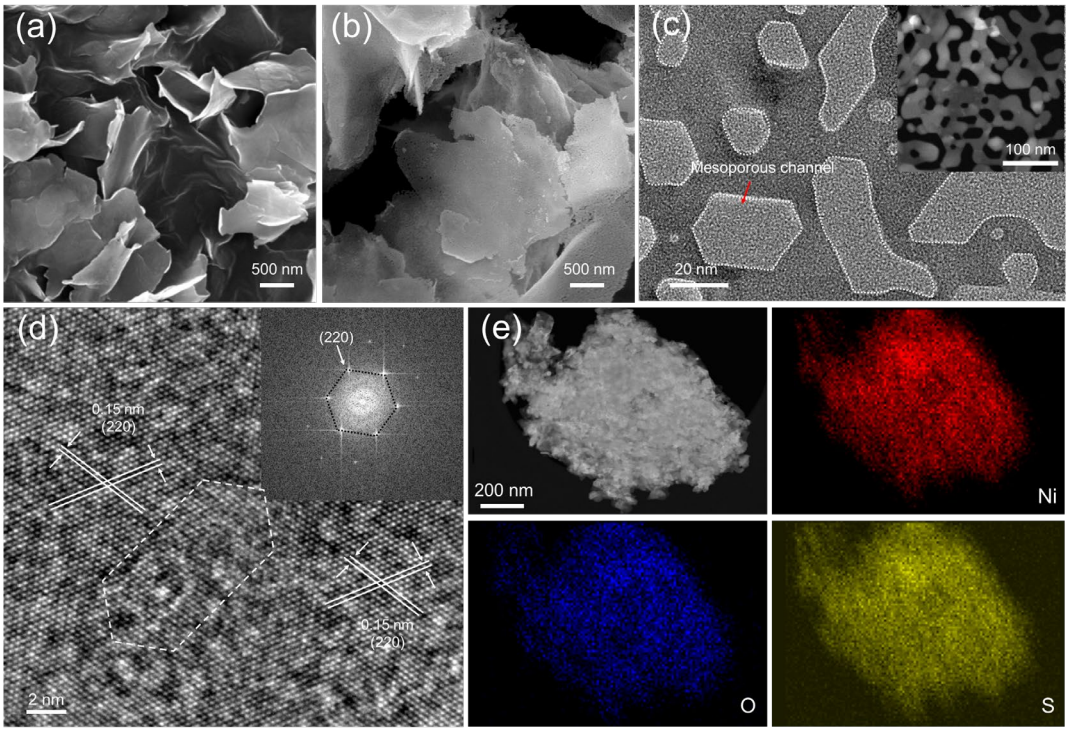

Fig. 1 (a) SEM image of sheet-like Ni-based precursor; (b) SEM image of NNN sample; (c) TEM image and HAADF-STEM image (inset) of NNN sample; (d) HRTEM image of NNN sample and the corresponding FFT of the selected area; (e) STEM image of NNN-S80 and the corresponding EDS mapping images.

To maximum the contact, the NNN and S samples were first grinded in agate mortar and then transferred into a sealed Teflon-lined autoclave at a proper temperature to ensure a homogenous distribution of S on NNN (see Experimental Section). After that, the NNN-S80 composite was characterized via XRD analysis (Fig. S1), where the NiO was maintained the cubic structure and the other diffraction peaks was verified to be orthorhombic of S (Reference code: 01-085-0799). The specific weight percentage of S in the NNN-S composites were analyzed via TGA measurement. As can be seen from Fig. S3, the sharp decrease of the weight percentage from 150 ℃ to 300 ℃ is corresponding to the sublimation of S, and after this process, the specific weight percentage of S contents were measured to be 85%, 65%, 43% and 22%, which are close to the nominal ratio. The TEM images (Fig. S4a and b) showed the morphology of NNN-S80 and NNN-S40 samples, respectively, which revealed that the S is not existed alone but distributed on the NNN sample compared with the TEM image in Fig. 1c. In order to confirm the distribution of elemental S in the NNN-S80 composite, STEM image and the corresponding EDS elemental mapping of Ni, O and S are displayed in Fig. 1e. The elemental distribution maps on an integrate NNN-S80 sheet revealed the uniform distribution of S, Ni and O elements. Compared with the STEM image and EDS maps of NNN-S20 in Fig. S4c, the relative contents of the S for NNN-S80 is higher than NNN-S20, which can be distinguished via the strength of S signal. The HRTEM in Fig. S5 showed the multi-group of lattice fringes, in which the inter-planar spacing between adjacent fringes (red line box) are measured to be 0.39 nm and 0.24 nm from two orientations, corresponding to the characteristic (222) plane and (422) plane, respectively. Meanwhile, the inter-planar spacing between adjacent fringes (green line box) are measured to be 0.58 nm and 0.24 nm from two orientations, corresponding to the (113) and (422) planes, respectively. The excellent crystal structure of S after sealed Teflon-lined autoclave approach from the HRTEM

image and XRD pattern indicate that the S was maintained its origin structure when experienced pre-processing.

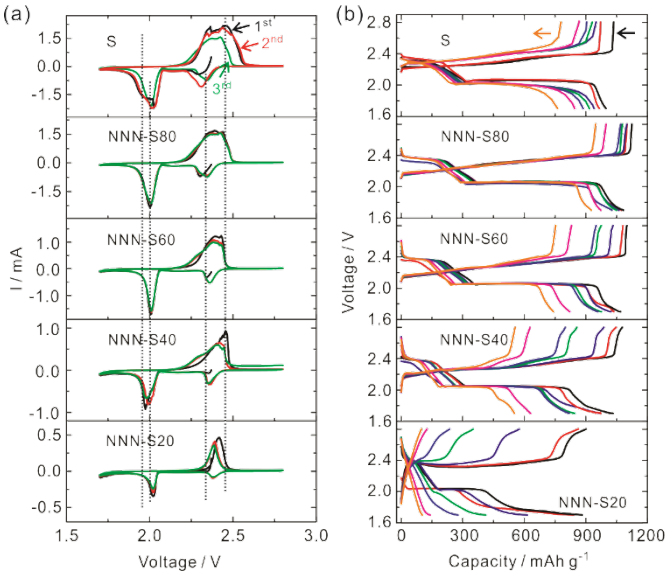

Fig. 2 (a) The first three cycles CV curves of NNN-S20, NNN-S40, NNN-S60, NNN-S80, S, and their corresponding discharging /charging curves (b), the cycle numbers are 1st, 2nd, 5th, 10th, 20th, 30th and 50th from right to left, respectively.

To reveal the mechanisms of the interaction between S and NiO, optimize the loading of S in the NNN-S composites for a Li-S cell, CV measurements and discharging/charging reaction were investigated. The first three cycles of CV curves for the NNN-S samples and S (with carbon layer at the cathode side) were obtained at a scan rate of 0.05 mV s^{-1} from 3.0 to 1.5 V which can be seen in Fig. 2a. Typical for S sample, the reduction peaks around 2.20 - 2.40 V are corresponding to the reduction of S_8 to soluble high order Li_2S_n ($4 \le n \le 8$), while the peaks around 2.05 V are corresponds to the further reduction of the high-order Li_2S_n to Li_2S_2 and eventually, to Li_2S[10]. The two overlapped oxidation peaks between 2.2 and 2.5 V, are corresponding to the transformation of short-chain polysulfides to S_8/Li_2S_8[39, 40]. Compared with the CV curves of S, NNN-S80, NNN-S60, NNN-S40 and NNN-S20 exhibited only two reduction peaks at around 2.30 V and 2.05 V, which indicated the simplified reduction steps from S_8 to Li_2S_2 and eventually, to Li_2S. The gradually decrease of reduction and oxidation peak current intensity from NNN-S80 to NNN-S20 may be attributed to the lowering of S content and high interaction between NiO and polysulfides. The discharging/charging curves of S, NNN-S80, NNN-S60, NNN-S40 and NNN-S20 at 0.2 C rate (the 1 C-rate is defined as the current density of 1675 mA g^{-1}) are shown in Fig. 2b, where the seven pairs of discharging/charging curves from right to left are corresponding to the 1st, 2nd, 5th, 10th, 20th, 30th and 50th cycles, respectively. Among the five samples, the S-cell with carbon layer at the cathode side of the separator exhibited much higher discharging/charging stability than the pure S-cell (S NL, Fig. S6), indicating that the existence of carbon layer can effectively prevent the polysulfides from "shuttling" to the anode. Meanwhile, the cycling stability of the NNN-S80 cell without a carbon layer at the cathode side (NNN-S80 NL) of the separator also showed relative better cycling performance and Coulombic efficiency than S NL at 0.2 C rate (Fig. S6), but relative poor than NNN-S80 cell coordinated with a carbon layer (Fig. 2b), and suffered from obvious capacity decrease after 50th cycle. Besides, NNN-S80, NNN-S60 and NNN-S40 exhibited the highest initial discharge capacity (~ 1100 mAh g^{-1}), while NNN-S60, NNN-S40 and NNN-S20 showed significant capacity loss with the increasing of cycle numbers. It should be noted that the cycling stability of the NNN-S80 cell is further enhanced compared with S-cell after adding carbon layer at the cathode side of the separator. Thus, 80 wt% S loading on NNN sample can be ascribed to deliver excellent Li-S storage performance. As can be seen from the XRD pattern in Fig. S7, the NiO still maintained its original crystal structure after 50th cycling, indicating that NiO can be stabilized in a Li-S cell.

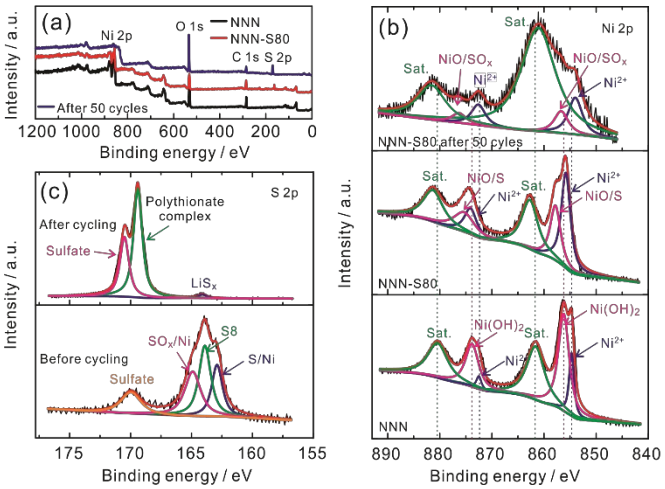

Fig. 3 (a) Full-range XPS spectrum and high-resolution Ni 2p spectrum (b) of NNN, NNN-S80 and NNN-S80 after 50th cycles at a discharge/charge rate of 0.2 C; (c) high resolution S 2p spectrum of NNN-S80 sample before and after 50th cycles at 0.2 C.

XPS characterization was also conducted in order to investigate the surface composition and valence change by adding S before and after cycling. The full-range XPS spectrum (Fig.3a) of NNN, NNN-S80 and NNN-S80 after 50th cycles at 0.2 C showed obvious characteristic peaks of C 1s, O 1s, S2p (except NNN sample) and Ni 2p, indicating the existence of the C, O, S and Ni elements on the surface of NiO sheets. In order to precisely understand the valence change for Ni and S, the high resolution Ni 2p and S 2p peaks were fitted which can be seen in Fig. 2b-c. As for NNN sample, peaks located at 854.7 eV and 872.5 eV are corresponding to the Ni^{2+} for NiO,[41] 856.2 eV and 873.8 eV are represent the Ni^{2+} for $Ni(OH)_2$,[42] while peaks located at 861.6 eV and 880.4 eV are characteristic satellite peaks of NiO.[43] After loading S on the NNN sample, the O-S interaction result in peak shifting to higher binding energy orientation, where the relative peak intensity of NiO (855.8 eV and 874.1 eV) was increased compared with NNN sample due to the decomposition of $Ni(OH)_2$ on the surface. Meanwhile, the peaks located at 855.8 eV and 875.3 eV are corresponding to the NiO/S

species which elevated the valence of Ni in some extent.[44, 45] In comparison, the Li-S cell by using NNN-S80 as cathode after 50th cycles at discharge/charge rate of 0.2 C showed relative higher satellite peaks (861.1 eV and 881.6 eV) when compared with other fitted peaks, which may be ascribed to the coverage of polythionate complex on the surface. Meanwhile, the XRD pattern in Fig. S7 showed that after discharging/charging performance, the NNN sample still maintained the cubic structure with ignored S signals detected which revealed that the crystal S has decomposed and transferred to other forms of S-based states. Apart from the Ni 2p spectrum, the high-resolution XPS spectrum of S 2p for NNN-S80 sample before and after cycling process have been fitted, which can be seen in Fig. 4c. Before cycling, the S was deconvoluted into four peaks, where peaks located at 162.9 eV, 164.0 eV and 165.0 eV are corresponding to the S/Ni interaction, S8 and SO_x/Ni interaction.[46, 47] The existing interaction of Ni with S and SO_x would help to prevent the S based species from "shuttle" to the anode during Li-S battery operation. The S 2p peak at 167.4 eV is corresponding to the binding energy of sulfate, which may arise from a surface oxidation exposed in air. After cycling, the fitted XPS peak at 168.3 eV was assigned to polythionate complex, which was formed during redox process due to the strong interaction at the surface.[28, 48]

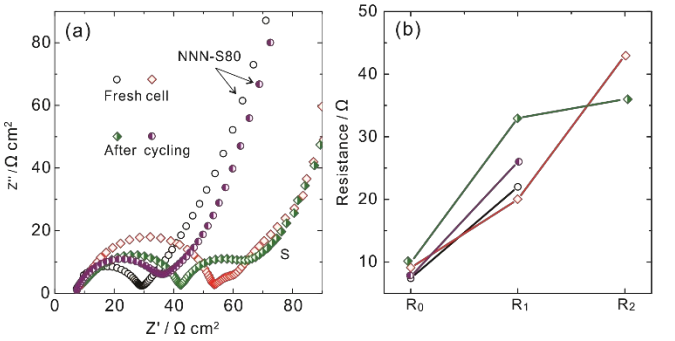

Figure 4. (a) Nyquist plots S and NNN-S80 electrodes before and after 50th cycles, (b) the corresponding resistance parameters and equivalent circuit diagram (inset).

To gain better understanding of the effectiveness by using network NiO sheets and carbon coating on the cathode side of separator in improving the performance of the Li–S battery, EIS of the NNN-S80 and S electrodes were measured and shown in Fig. 4. The Nyquist plots (Fig. 4a) for S electrode consist of two semicircles in the high–medium frequency region and a sloped line in the low frequency region, which are related to the impedance of passivation film (R_2), charge transfer resistance (R_1), and semi-in finite Warburg diffusion process, respectively.[49-51] It is difficult to distinct a semicircle related to passivation film impedance for NNN-S80 electrode, indicating better electrolyte infiltration, and thereby mitigating the formation of the passivation layer (Li_2S_2/Li_2S) on the lithium anodes. The EIS plots were fitted via two kinds of equivalent circuit diagram (inset of Fig. 4b), where the upper one represents the S-cell and bottom one is the NNN-S80 cell, and the relative resistance parameters were plotted in Fig. 4b. In detail, the R1 value of NNN-S80 is near equal to S electrode for a fresh cell, and after 50th cycles, the increasing of R1 value of NNN-S80 electrode his much smaller than S electrode. Besides, the formation of passivation film for a S-cell contained a relative large resistance which, in some extent, increased the interface transmission impedance of Li^+, and then reduced the overall system dynamics. The improved polysulfides-entrapment capacity verifies that NNN-S80 electrode configuration is more promising to solve the persistent problem of capacity fade.

Subsequently, the NNN-S80 and S cells were evaluated by galvanostatic discharge/charge at various current rates. As shown in Fig. 5a, the NNN-S80 exhibited excellent rate performance. At the rate of 0.2 C, it delivered a high specific discharge capacity of 1231 mAh g^{-1} with a coulombic efficiency of 99.5%, which is higher than S (1025 mAh g^{-1}, 91.4%). The capacity faded slowly in the subsequent cycles, the rate was increased to 0.5 C, a specific capacity of 1050 mAh g^{-1} was retained, which then slowly reduced to 890 mAh g^{-1} at 1 C, 801 mAh g^{-1} at 2 C, and 696 mAh g^{-1} at 5C, before it finally recovered to 996 mAh g^{-1} at 0.2 C after 10 cycles. In comparison, the capacity changing of S cell suffered a huge gap with NNN-S80, where the capacity at discharging rate of 0.5 C, 1 C, 2 C and 5 C is 875 mAh g^{-1}, 746 mAh g^{-1}, 687 mAh g^{-1} and 436 mAh g^{-1}, respectively, especially, the value difference of discharging capacity between NNN-S80 and S at 5 C is 260 mAh g^{-1}, indicating the excellent rating performance of NNN-S80. Furthermore, both the discharge and charge capacities were stable at different current densities and the coulombic efficiency was almost 100%, suggesting a perfect control of the so-called shuttle effect, which is regarded as the biggest disadvantage of a Li-S battery.

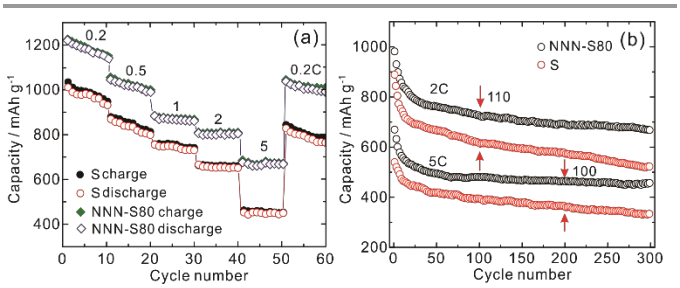

Fig. 5 (a) Rate performance of NNN-S80 and S cells ranging from discharge/charge rate of 0.2 to 5 C; (b) Long-term discharge stability tests of NNN-S80 and S cells at 2 C and 5 C.

To evaluate the efficiency of the mediator, long-term cycling capability was performed at discharging/charging rates of 2 C and 5 C for NNN-S80 and S samples. As can be seen from Fig. 5b, the as-prepared cell with a rechargeable rate of 2 C showed excellent first discharge capacity of 992 mAh g^{-1}, and retained at 756 mAh g^{-1} after 50 cycles. At the 100th cycle, the capacity value gap between NNN-S80 and S cell was ca. 110 mAh g^{-1}, indicating that the addition of NNN effectively not only enhanced the durability, but also effectively hindered the dissolution of polysulfides during discharging/charging process. After 300 cycles, there are still 682 mAh g^{-1} maintained and a very low decay rate of 0.104% per cycle. Besides, the NNN-S80 cell also exhibited superior durability at high discharging/charging rate of 5 C (Fig. 5b). At the 200th cycle, the capacity value gap between NNN-S80 and S cell was ca. 100 mAh g^{-1}, and after 300 cycles, there are still 432 mAh g^{-1} maintained, coordinated with the cycling performance at 2 C, the addition of NNN was recommended to effectively improved the battery

performance at high discharging/charging rates. In addition, the difference in capacity gap between the rate performance and long-term cycling performance may be ascribed by the initial activation of at low discharging/charging rates in the rate performance.

Conclusions

In summary, NiO with network structure was very effective to entrap polysulfides in a Li-S battery when coupled with a thin carbon film on the cathode side of the separator. On the basis of porous network structure and interaction with S, the battery performance was further enhanced. Specifically, by introducing a thin carbon layer on the cathode side of the separator, the dissolution of polysulfides was effectively hindered and the rate capability and long-term stability was effectively enhanced by further addition of network NiO nanosheets. Compared with the Li-S cell performance with different S loading, the cathode with 80 wt% of S in the total electrode exhibited a high specific capacity and excellent rate performance up to 5 C. In addition, although the redox potential range of NiO is not involved in the rechargeable potential window, NiO exhibit obvious interaction with polysulfides and restricted its dissolution tendency. The present study thus demonstrates that the joint action of network NiO and carbon layer shows great potential to be used in low-cost and high-energy Li–S batteries and provides important guidance to the design of a multi-functional sulfur host for Li–S batteries.

Acknowledgements

This work was supported by the National Natural Science Foundation (21573083), 1000 Young Talent (to Deli Wang), and the Innovation Research Funds of Huazhong University of Science and Technology (2017KFYXJJ164). The authors thank the Analytical and Testing Center of HUST for XRD, STEM measurements. S/TEM work was carried out at the Department of applied physics, The Hong Kong Polytechnic University, which are supported by the Hong Kong Research Grants Council through the Early Career Scheme (Project No. 25301617) and the Hong Kong Polytechnic University grant (Project No. 1-ZE6G). J.W., X.G. and Y.Z. thanks Dr. Lu Wei for optimizing the JEOL JEM-2100F microscope.

Notes and references

1. S. Evers and L. F. Nazar, *Accounts Chem. Res*., 2013, **46**, 1135-1143.
2. L. F. Nazar, M. Cuisinier and Q. Pang, *MRS Bull*., 2014, **39**, 436-442.
3. Y. Yang, G. Zheng and Y. Cui, *Chem. Soc. Rev.*, 2013, **42**, 3018-3032.
4. X. Tao, Y. Liu, W. Liu, G. Zhou, J. Zhao, D. Lin, C. Zu, O. Sheng, W. Zhang and H.-W. Lee, *Nano Lett.*, 2017, **17**, 2967-2972.
5. Q. Fan, W. Liu, Z. Weng, Y. Sun and H. Wang, *J. Am. Chem. Soc.*, 2015, **137**, 12946-12953.
6. J. Jiang, J. Zhu, W. Ai, X. Wang, Y. Wang, C. Zou, W. Huang and T. Yu, *Nat. Commun.*, 2015, **6**, 8622.
7. D. Larcher and J.-M. Tarascon, *Nat. Chem.*, 2015, **7**, 19-29.
8. Q. Pang, D. Kundu, M. Cuisinier and L. Nazar, *Nat. Commun.*, 2014, **5**, 4759.
9. X. Tao, J. Wang, C. Liu, H. Wang, H. Yao, G. Zheng, Z. W. Seh, Q. Cai, W. Li and G. Zhou, *Nat. Commun.*, 2016, **7**, 11203.
10. X. Ji, K. T. Lee and L. F. Nazar, *Nat. Mater.*, 2009, **8**, 500-506.
11. J. Schuster, G. He, B. Mandlmeier, T. Yim, K. T. Lee, T. Bein and L. F. Nazar, *Angew. Chem.*, 2012, **124**, 3651-3655.
12. J. Wang, S. Chew, Z. Zhao, S. Ashraf, D. Wexler, J. Chen, S. Ng, S. Chou and H. Liu, *Carbon*, 2008, **46**, 229-235.
13. Y.-S. Su and A. Manthiram, *Nat. Commun.*, 2012, **3**, 1166.
14. Y.-P. Xie, H.-W. Cheng, W. Chai, H. Yue, X. Zhang, J.-H. Fang, H.-B. Zhao and J.-Q. Xu, *Chinese Chem. Lett.*, 2017, **28**, 738-742.
15. N. Jayaprakash, J. Shen, S. S. Moganty, A. Corona and L. A. Archer, *Angew. Chem.*, 2011, **123**, 6026-6030.
16. G. Zhou, Y. Zhao and A. Manthiram, *Adv. Energy Mater.*, 2015, **5**, 1402263.
17. W. Zhou, C. Wang, Q. Zhang, H. D. Abruña, Y. He, J. Wang, S. X. Mao and X. Xiao, *Adv. Energy Mater.*, 2015, **5**, 1401752.
18. D. Wang, Y. Yu, W. Zhou, H. Chen, F. J. DiSalvo, D. A. Muller and H. D. Abruña, *Phys. Chem. Chem. Phys.*, 2013, **15**, 9051-9057.
19. J. Guo, Y. Xu and C. Wang, *Nano Lett.*, 2011, **11**, 4288-4294.
20. L. Yuan, H. Yuan, X. Qiu, L. Chen and W. Zhu, *J. Power Sources*, 2009, **189**, 1141-1146.
21. W. Ahn, K.-B. Kim, K.-N. Jung, K.-H. Shin and C.-S. Jin, *J. Power Sources*, 2012, **202**, 394-399.
22. G. Zheng, Y. Yang, J. J. Cha, S. S. Hong and Y. Cui, *Nano Lett.*, 2011, **11**, 4462-4467.
23. J. Wang, J. Yang, J. Xie and N. Xu, *Adv. Mater.*, 2002, **14**, 963-965.
24. Y. Yang, G. Yu, J. J. Cha, H. Wu, M. Vosgueritchian, Y. Yao, Z. Bao and Y. Cui, *ACS Nano*, 2011, **5**, 9187-9193.
25. G. C. Li, G. R. Li, S. H. Ye and X. P. Gao, *Adv. Energy Mater.*, 2012, **2**, 1238-1245.
26. C. J. Hart, M. Cuisinier, X. Liang, D. Kundu, A. Garsuch and L. F. Nazar, *Chem. Commun.*, 2015, **51**, 2308-2311.
27. D.-W. Wang, Q. Zeng, G. Zhou, L. Yin, F. Li, H.-M. Cheng, I. R. Gentle and G. Q. M. Lu, *J. Mater. Chem. A*, 2013, **1**, 9382-9394.
28. X. Liang, C. Hart, Q. Pang, A. Garsuch, T. Weiss and L. F. Nazar, *Nat. Commun.*, 2015, **6**, 5682.
29. Z. Li, J. Zhang and X. W. D. Lou, *Angew. Chem. Int. Ed.*, 2015, **54**, 12886-12890.
30. X. Liang, C. Y. Kwok, F. Lodi‐Marzano, Q. Pang, M. Cuisinier, H. Huang, C. J. Hart, D. Houtarde, K. Kaup and H. Sommer, *Adv. Energy Mater.*, 2016, **6**, 1501636.
31. J.-Q. Huang, Q. Zhang and F. Wei, *Energy Storage Mater.*, 2015, **1**, 127-145.
32. T. Z. Zhuang, J. Q. Huang, H. J. Peng, L. Y. He, X. B. Cheng, C. M. Chen and Q. Zhang, *Small*, 2016, **12**, 381-389.
33. M. S. Kim, L. Ma, S. Choudhury and L. A. Archer, *Adv. Mater. Interfaces*, 2016, **3**, 1600450.
34. Y. Xiang, J. Li, J. Lei, D. Liu, Z. Xie, D. Qu, K. Li, T. Deng and H. Tang, *ChemSusChem*, 2016, **9**, 3023-3039.
35. X. Wang, G. Li, J. Li, Y. Zhang, A. Wook, A. Yu and Z. Chen, *Energy Environ. Sci.*, 2016, **9**, 2533-2538.

36. K. Xu, P. Chen, X. Li, Y. Tong, H. Ding, X. Wu, W. Chu, Z. Peng, C. Wu and Y. Xie, *J. Am. Chem. Soc.*, 2015, **137**, 4119-4125.
37. G. Li, J. Sun, W. Hou, S. Jiang, Y. Huang and J. Geng, *Nature Commun.*, 2016, **7**, 10601.
38. J. Balach, T. Jaumann, M. Klose, S. Oswald, J. Eckert and L. Giebeler, *Adv. Funct. Mater.*, 2015, **25**, 5285-5291.
39. Y. Fu, Y. S. Su and A. Manthiram, *Angew. Chem.*, 2013, **125**, 7068-7073.
40. H. Yamin, A. Gorenshtein, J. Penciner, Y. Sternberg and E. Peled, *J. Electrochem. Soc.*, 1988, **135**, 1045-1048.
41. E. Khawaja, M. Salim, M. Khan, F. Al-Adel, G. Khattak and Z. Hussain, *J. Non-cryst. Solids*, 1989, **110**, 33-43.
42. Y.-Z. Su, K. Xiao, N. Li, Z.-Q. Liu and S.-Z. Qiao, *J. Mater. Chem. A*, 2014, **2**, 13845-13853.
43. A. Mansour, *Surf. Sci. Spectra*, 1994, **3**, 231-238.
44. J. Liu, J. Lu, P. Chu and J. Blakely, *J. Vac. Sci.Technol. A*, 1992, **10**, 2355-2360.
45. J. Matienzo, L. I. Yin, S. O. Grim and W. E. Swartz Jr, *Inorg. Chem.*, 1973, **12**, 2762-2769.
46. T. Yokoyama, A. Imanishi, S. Terada, H. Namba, Y. Kitajima and T. Ohta, *Surf. Sci.*, 1995, **334**, 88-94.
47. Y. Diao, K. Xie, S. Xiong and X. Hong, *J. Power Sources*, 2013, **235**, 181-186.
48. B. Lindberg, K. Hamrin, G. Johansson, U. Gelius, A. Fahlman, C. Nordling and K. Siegbahn, *Phys. Scripta*, 1970, **1**, 286.
49. X.-Q. Niu, X.-L. Wang, D. Xie, D.-H. Wang, Y.-D. Zhang, Y. Li, T. Yu and J.-P. Tu, *ACS Appl. Mater. Interfaces*, 2015, **7**, 16715-16722.
50. J. Yang, J. Xie, X. Zhou, Y. Zou, J. Tang, S. Wang, F. Chen and L. Wang, *J. Phys. Chem. C*, 2014, **118**, 1800-1807.
51. M. Li, W. Wahyudi, P. Kumar, F. Wu, X. Yang, H. Li, L.-J. Li and J. Ming, *ACS Appl. Mater. Interfaces*, 2017, **9**, 8047-8054.